Load redistribution in eutectic high entropy alloy AlCoCrFeNi<inf>2.1</inf> during high temperature deformation

Materialia 22 (2022) 101392

Contents lists available at ScienceDirect

Materialia

journal homepage: www.elsevier.com/locate/mtla

Full Length Article

Load redistribution in eutectic high entropy alloy $AlCoCrFeNi_{2.1}$ during high temperature deformation

Nitesh Raj Jaladurgam[a], Adrianna Lozinko[b], Sheng Guo[b], Stefanus Harjo[c], Magnus Hörnqvist Colliander[a,*]

[a] Department of Physics, Chalmers University of Technology, Gothenburg SE-41296, Sweden
[b] Department of Industrial and Materials Science, Chalmers University of Technology, Gothenburg SE-41296, Sweden
[c] J-PARC Center, Japan Atomic Energy Agency, Japan

ARTICLE INFO

Keywords:
In-situ neutron diffraction
Eutectic high entropy alloy
Load distribution
Elastic lattice strains

ABSTRACT

The load redistribution between and within phases in eutectic high entropy alloy $AlCoCrFeNi_{2.1}$ was measured using in-situ neutron diffraction during tensile deformation at 973 K. The load partitioning between phases is reversed compared to lower temperatures, with $L1_2$ becoming the stronger phase. The evolution of the orientation-specific stresses and strains in the $L1_2$ phase suggests that cube slip dominates the response. The low strength, internal load transfer and ideally plastic response of the B2 phase indicate a change in deformation mechanism compared to lower temperatures.

1. Introduction

To resolve the issues with pronounced strength-ductility trade-off in single phase high entropy alloys (HEAs) and address the inferior castability and compositional segregation, Lu et al. [1] introduced *eutectic* HEAs (EHEAs). EHEAs exhibit good thermal stability and the regular lamellar or rod-like eutectic microstructures provide excellent mechanical properties [2]. The alloy proposed in [1], $AlCoCrFeNi_{2.1}$, presents a lamellar microstructure of ordered $L1_2$ and B2 phases with Kurdjumov–Sachs orientation relationship [3–7], and shows an excellent combination of strength and ductility from cryogenic to elevated temperatures [1,8–10]. Nano and micromechanical testing of individual phases and phase boundaries at room temperature have shown that $L1_2$ is the softer phase, with B2 acting as strengthener [11]. The phase boundaries are crack resistant as a result of the promotion of slip activity in the hard B2 phase by large dislocation pile-ups at the interphase boundaries [12]. During deformation the interaction between phases leads to pronounced load transfer from $L1_2$ to B2 [13]. With increasing temperature up to 673 K the degree of load transfer is reduced, and at room temperature and above a transition from octahedral $<011>\{111\}$ slip to $<011>\{001\}$ cube slip occurred [13]. In this work we report that at even higher temperatures (973 K) a change in the behaviour of the B2 phase leads to an inverse load partitioning compared to at lower temperatures, with $L1_2$ acting as the reinforcing phase. The results points to the need for thorough investigations of the dominating deformation mechanisms in both B2 and $L1_2$ phases as a function of temperature and strain rate in order to fully understand and exploit the individual phase properties during microstructure optimisation.

2. Materials and methods

The as-cast lamellar microstructure of the $AlCoCrFeNi_{2.1}$ EHEA, shown in Fig. 1(a), has been extensively studied with respect to chemical composition and crystal structure of the phases [3,4,12,14]. The previously reported ordered $L1_2$ and B2 structures have been confirmed for the particular batch studied here, with a B2 volume fraction $v_f \approx 0.35$, and the chemical composition of the phases were reported to be (in at.%) 11Al-18Co-21Cr-19Fe-31Ni ($L1_2$) and 21Al-15Co-14Cr-15Fe-35Ni (B2) [13]. In-situ tensile tests were performed at the time-of-flight engineering materials diffractometer TAKUMI, J-PARC, Japan. A detailed description of the setup can be found in [15]. Diffraction patterns were collected with the diffraction vector aligned with the tensile axis in order to measure strains in this direction. Samples were heated to 973 K and stabilized for 30 minutes, followed by continuous loading at a constant strain rate of 10^{-6} s^{-1} during which diffraction signals were recorded. In order to confirm comparability between previous results [13] and the present study, an additional sample was tested at room temperature, see Fig. S 1 in Supplementary Material. We focus on the behaviour around yielding and early stages of plasticity, and the test was therefore stopped at a total strain around 1 %. A representative diffractogram of $AlCoCrFeNi_{2.1}$ with fundamental Bragg peaks from $L1_2$ and B2 phases marked (superlattice peaks were too weak to be reliably fitted) is shown

* Corresponding author.
E-mail address: magnus.colliander@chalmers.se (M.H. Colliander).

https://doi.org/10.1016/j.mtla.2022.101392
Received 13 December 2021; Accepted 12 March 2022
Available online 16 March 2022

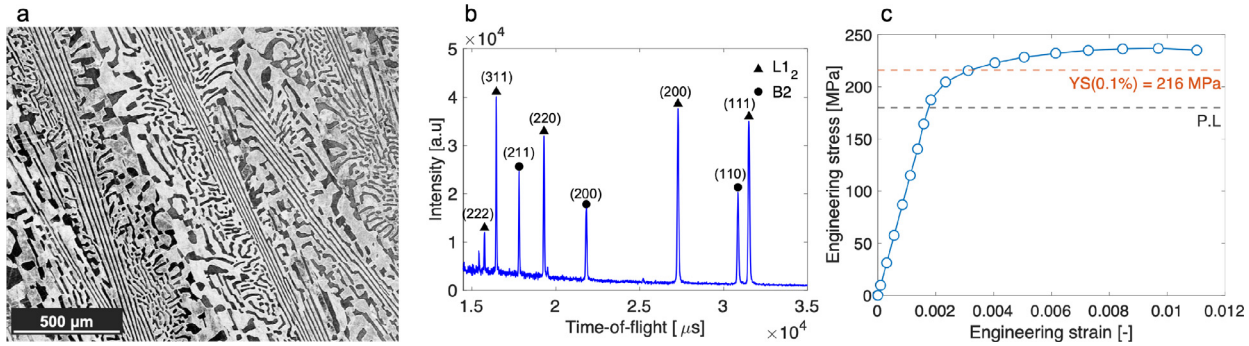

Fig. 1. (a) The microstructure of $AlCoCrFeNi_{2.1}$ with ordered $L1_2$ B2 phases; (b) Representative neutron time-of-flight diffractogram and (c) macroscopic stress-strain curve at 973 K with yield stress of 216 MPa.

in Fig. 1(b). Individual peaks were fitted with convoluted back-to-back exponentials and pseudo-Voigt shape function using GSAS-II [16]. The orientation-specific lattice strain for each $\{hkl\}$ peak was calculated as $\epsilon_{hkl} = d^{hkl}/d_0^{hkl} - 1$, where d^{hkl} is the measured interplanar spacing under load and d_0^{hkl} is the unloaded reference. The phase-averaged elastic strain of each phase, ϵ_p, was calculated as the multiplicity-weighted average of the individual peaks [17].

3. Results and discussion

Figure 1(c) shows the macroscopic stress–strain curve. The yield strength (0.1 % proof stress) is measured to be 216 MPa, which is considerably lower than previously reported values (550 MPa) for as-cast $AlCoCrFeNi_{2.1}$ at the same temperature [10]. We have previously reported good agreement between the stress–strain response of the current material batch with literature data at 77 and 293 K, as well as ex-situ tests at 293 and 673 K [13], and therefore believe that the measured values are correct. The reasonable elastic modulus of both bulk material and individual phases, see Fig. S 2 in Supplementary Material, further supports this. The discrepancy could be due to the very slow strain rate (10^{-6} s^{-1}) employed to allow continuous diffraction measurements with sufficient accuracy, which could in turn enable time-dependent deformation. Comparing deformation conditions in terms of the Zener-Hollomon parameter using the activation energy 336 kJ·mol^{-1} [18], a decrease from 10^{-3} to 10^{-6} s^{-1} at 973 K corresponds to an increase in temperature to 1167 K at a strain rate of 10^{-3} s^{-1}. Consequently a considerable decrease in yield strength can be expected due to the lower strain rate applied in the present work. In light of these values the present yield strength of 216 MPa appears realistic. After yielding the flow stress remains approximately constant, without pronounced work hardening.

The evolution of phase-averaged elastic lattice strains in Fig. 2(a) show that after the initial elastic (linear) region, where the response is similar in the two phases, the curves separate and larger strains are accumulated by the $L1_2$ phase. As the measured lattice strains are elastic and therefore directly proportional to stress, this indicates a load transfer from B2 to $L1_2$ upon yielding, contrary to previous observations in the temperature range 77–673 K [13]. This is confirmed by the corresponding phase-averaged stresses ($\sigma_p = E_p\epsilon_p$, where p denotes the phase and E_p is the effective stiffness, which is calculated from the slope of the macroscopic stress against ϵ_p in the elastic regime, see Fig. S 2 in Supplementary Material) in Fig. 2(b) where σ_{L1_2} is considerably higher than σ_{B2}. This indicates that, at least under the slow strain rate conditions employed here, the roles of the phases become reversed at higher temperatures, leaving $L1_2$ to be the hard reinforcing phase instead of B2. Closer inspection of the phase-specific stresses in Fig. 2(b) shows that there is a small amount of work hardening in the $L1_2$ phase, whereas the the B2 phase behaves almost ideally plastic. The average stress according to the rule-of-mixture (ROM), $\bar{\sigma} = (1 - v_f)\sigma_{L1_2} + v_f\sigma_{B2}$, agrees well with the measured stress from the load cell, see Fig. 2(b).

To further understand the behaviour we examine the orientation-specific lattice strain and stress evolution. Here we note that the orientation-specific stresses ($\sigma_p^{hkl} = E_p^{hkl}\epsilon_p^{hkl}$) were obtained using effective stiffnesses calculated in the same way as for the phase-averaged case above, i.e. from the slope of the macroscopic stress against ϵ_p^{hkl} (see Fig. S 2 in Supplementary Material). This approach implicitly assumes the same stress in all grains (the Reuss approximation), which cannot be strictly true due to the elastic anisotropy and interactions. This causes the collapse of the σ_p^{hkl} for different orientations to a single curve in the elastic region in Fig. 2(g,h), which should not be taken to mean that the stress is actually the same in all orientations. The orientation-specific stress does, on the other hand, serve to highlight the difference in response of individual orientations in the plastic regime.

We observe early yielding of the grains oriented with (111) planes normal to the tensile axis in $L1_2$, indicated by the increasing slope after onset of plasticity Fig. 2(c). As plastic deformation in these grains starts, they progressively loose the ability to carry stress and therefore accumulate less elastic strain (i.e. stress). This is similar to previous observations at 673 K [13], but even more pronounced, clearly indicating the occurrence of cube slip as the Schmid factor for octahedral slip in these grains are close to zero. The increasing rate of elastic lattice strain (i.e. increasing stress levels) in the grains oriented with (200), and to a lesser extent (311), planes normal to the tensile axis show that the load is preferentially transferred to these grains. The orientation-specific stresses, shown in Fig. 2(g) further confirms the occurrence of cube slip in $L1_2$, as seen from the low flow stress of the (111) orientation. The previously mentioned work hardening, which can be seen in $L1_2$ is primarily due to hardening of the (200) and (311) orientations, whereas the flow stress remains essentially constant in the (111) and (220) orientations.

The orientation-specific lattice strain evolution in B2 (Fig. 2(d,f)), on the other hand, differs significantly from previous observations at lower temperatures, where pronounced load transfer from (110) and (211) orientations to (200) occurred. The orientation-specific stresses in Fig. 2(h) show no appreciable load redistribution between orientations. This points to the need for further investigations into temperature dependence of the deformation mechanisms of the B2 phase in order to understand the difference in behaviour at 973 K compared to that at lower temperatures. A further point to consider is the orientation-dependent interactions between phases, which will inevitably arise from the Kurdjumov-Sachs orientation relationship. While out of the scope of the present study, elasto-plastic self-consistent (EPSC) simulations should be performed to investigate the effects of cube slip in the $L1_2$ phase on the load transfer to B2.

Zhang et al. [10] showed that extensive twinning occurred in the $L1_2$ lamellae during deformation of $AlCoCrFeNi_{2.1}$ at 973 K. Examining the propensity for twinning through the stacking fault probability, SFP, estimated from [19]

$$SFP = \frac{32\pi}{3\sqrt{3}}\left(\epsilon_{222} - \epsilon_{111}\right) \quad (1)$$

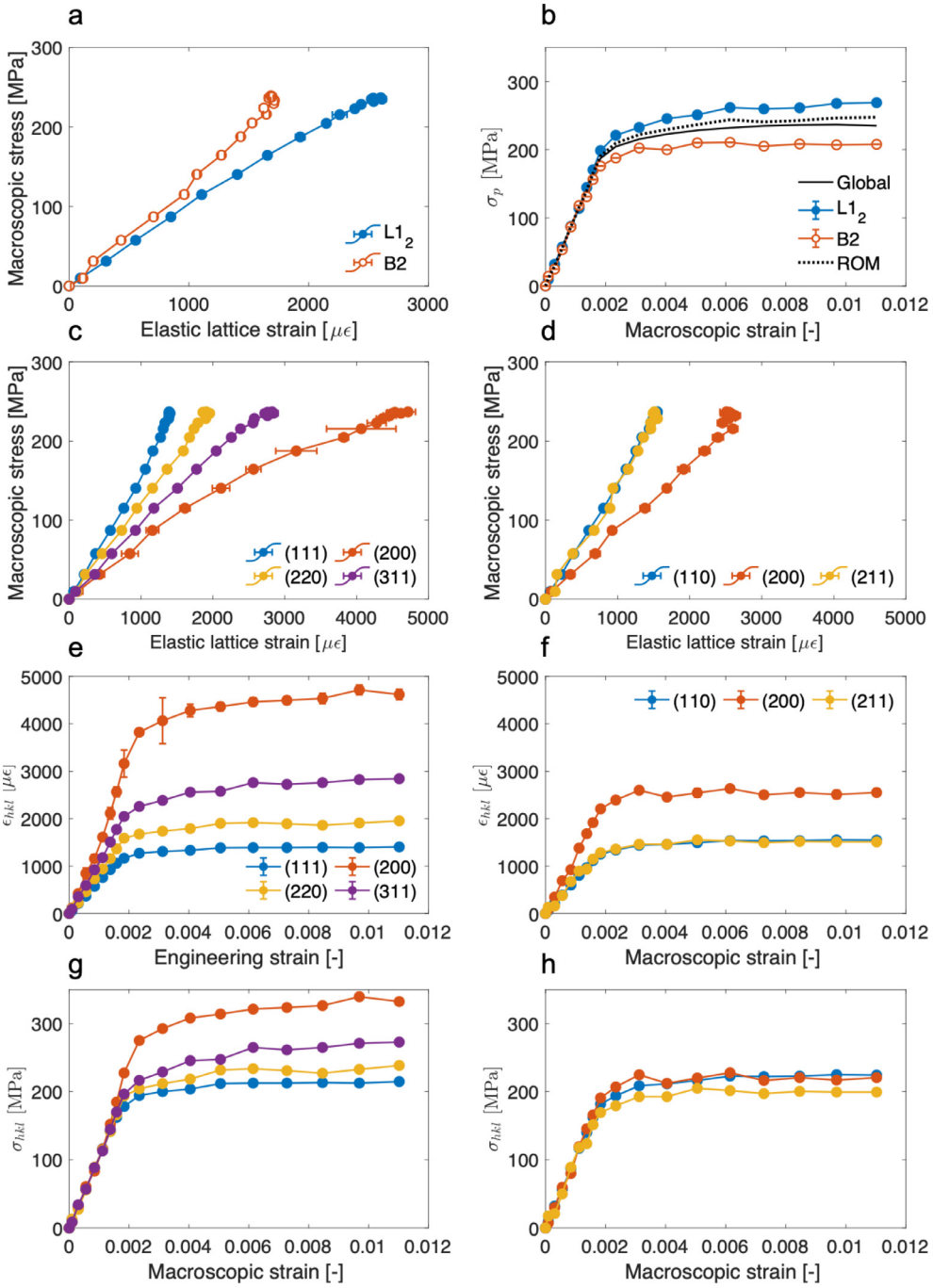

Fig. 2. The evolution of (a) phase-averaged lattice strain and (b) phase-averaged stress, including global and ROM stress. The evolution of orientation-specific lattice strains of (c,e) $L1_2$ and (d,f) B2, respectively. The orientation-specific stresses of (g) $L1_2$ and (h) B2.

we observe a small increase above the noise level at stresses around the yield stress (see Fig. 3). This could indicate the presence of twinning, although it is not expected to be extensive at the small strains in the present study. Notably, the SFP determined from the separate room temperature test used for data validation purposes did not increase after yielding (see Fig. S 3), suggesting that the above observation at 973 K is indeed a sign of twinning. However, diffraction from grains with $< 111 >$ aligned with the tensile direction does not present the most suitable condition for investigating SFP in alloys with cube slip. The (111) orientation is usually relatively prone to twinning since the Schimd factor for $< 112 > \{111\}$ twinning is slightly higher than for octahedral $< 011 > \{111\}$ slip. However, the Schmid factor for $< 011 > \{001\}$ cube slip is 1.5 times higher than that for twinning when loaded along (111), suggesting that such grains will undergo cube slip rather than twinning. Diffraction analysis of twinning in other orientations is not possible with the current experimental setup (fixed diffraction vector). We can also compare the lattice strain evolution of the $L1_2$ phase (Fig. 2(c)) to those reported by Wang et al. [20], from neutron diffraction studies of FeCoCrNi deformed in tension at 293 and 77 K. The amount of twinning was significantly higher at 77 K, shown by both transmission electron microscopy (TEM) and evolution of the SFP, but the lattice strain evolution did not show noticeable differences between temperatures. In particular, the order of yielding for the different orientations remained the same as expected in the presence of octahedral slip, contrary to observations from Fig. 2(a). Given the above discussion we conclude that while a certain amount of twinning cannot be ruled out, the dominat-

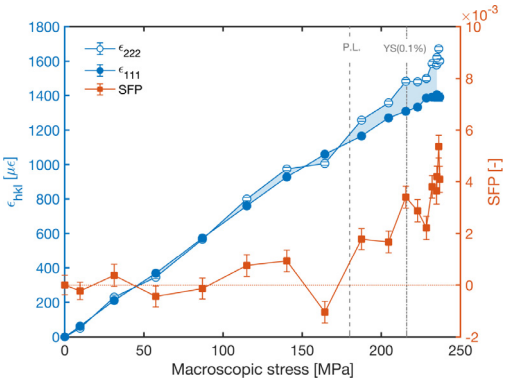

Fig. 3. Lattice strain evolution for the (111) and (222) peaks (left axis) and the resulting stacking fault probability (right axis) as function of macroscopic stress. The lines marked P.L. and YS(0.1%) mark the proportionality limit and the 0.1 % proof stress, respectively (see Fig. 1(a))

ing effects at the small strains investigated in this study arise from the $< 011 >\{001\}$ slip.

4. Conclusions

In conclusion, based on in-situ neutron diffraction measurements during tensile testing of an as-cast eutectic $L1_2$/B2 HEA ($AlCoCrFeNi_{2.1}$) at 973 K we report that:

- The load partitioning between phases is reversed compared to that at lower temperatures, causing $L1_2$ to become the stronger phase.
- The low strength, limited load transfer to the (200) orientation, and ideally plastic response of the B2 phase suggest a change in deformation mechanism compared to that at lower temperatures.
- The evolution of the orientation-specific stresses and strains in the $L1_2$ phase suggests that cube slip dominates the response.

In order to fully understand these observations, complementary TEM investigations must be carried out. Furthermore, the effects of strain rate on the above points should be carefully studied, and a thorough numerical investigation of the effects of orientation relationships on the interaction between the phases should be performed.

Declaration of Competing Interest

The authors declare that they have no known competing financial interests or personal relationships that could have appeared to influence the work reported in this paper.

Acknowledgment

This research is funded by the Swedish Foundation for Strategic Research (SSF) within the Swedish National Graduate School in Neutron Scattering (SwedNESS) with Grant number GSn15-0008, and was performed in part at the Chalmers Materials Analysis Laboratory, CMAL, and also got partially support from JSPS Kakenhi JP19H05180. Authors are grateful to Prof. Yiping Lu from School of Materials Science and Engineering, Dalian University of Technology, China for providing the EHEA material for this work. We thank Materials and Life Science Experimental Facility for the beamtime (2018B0117).

Supplementary material

Supplementary material associated with this article can be found, in the online version, at doi:10.1016/j.mtla.2022.101392.

References

[1] Y. Lu, Y. Dong, S. Guo, L. Jiang, H. Kang, T. Wang, B. Wen, Z. Wang, J. Jie, Z. Cao, H. Ruan, T. Li, et al., A promising new class of high-temperature alloys: Eutectic high-entropy alloys, Scientific Reports 4 (1) (2014) 6200, doi:10.1038/srep06200.
[2] Y. Lu, Y. Dong, H. Jiang, Z. Wang, Z. Cao, S. Guo, T. Wang, T. Li, P.K. Liaw, et al., Promising properties and future trend of eutectic high entropy alloys, Scripta Materialia 187 (2020) 202–209, doi:10.1016/j.scriptamat.2020.06.022.
[3] I.S. Wani, T. Bhattacharjee, S. Sheikh, Y.P. Lud, S. Chatterjee, P.P. Bhattacharjeea, S. Guo, N. Tsujib, Ultrafine-grained $AlCoCrFeNi_{2.1}$ eutectic high-entropy alloy, Materials Research Letters 4 (3) (2016) 174–179, doi:10.1080/21663831.2016.1160451.
[4] I.S. Wani, T. Bhattacharjee, S. Sheikh, P.P. Bhattacharjee, S. Guo, N. Tsuji, Tailoring nanostructures and mechanical properties of $AlCoCrFeNi_{2.1}$ eutectic high entropy alloy using thermo-mechanical processing, Materials Science and Engineering A 675 (2016) 99–109, doi:10.1016/j.msea.2016.08.048.
[5] Q. Wang, Y. Lu, Q. Yu, Z. Zhang, et al., The Exceptional Strong Face-centered Cubic Phase and Semi-coherent Phase Boundary in a Eutectic Dual-phase High Entropy Alloy AlCoCrFeNi, Scientific Reports 8 (1) (2018) 14910, doi:10.1038/s41598-018-33330-0.
[6] A. Lozinko, O.V. Mishin, T. Yu, U. Klement, S. Guo, Y. Zhang, Quantification of microstructure in a eutectic high entropy alloy $AlCoCrFeNi_{2.1}$, in: IOP Conference Series: Materials Science and Engineering, volume 580, IOP Publishing, 2019, p. 012039.
[7] A. Lozinko, Y. Zhang, O.V. Mishin, U. Klement, S. Guo, et al., Microstructural characterization of eutectic and near-eutectic AlCoCrFeNi high-entropy alloys, Journal of Alloys and Compounds 822 (2020) 153558, doi:10.1016/j.jallcom.2019.153558.
[8] T. Bhattacharjee, R. Zheng, Y. Chong, S. Sheikh, S. Guo, I.T. Clark, T. Okawa, I.S. Wani, P.P. Bhattacharjee, A. Shibata, N. Tsuji, et al., Effect of low temperature on tensile properties of $AlCoCrFeNi_{2.1}$ eutectic high entropy alloy, Materials Chemistry and Physics 210 (2018) 207–212, doi:10.1016/j.matchemphys.2017.06.023.
[9] Y. Lu, X. Gao, L. Jiang, Z. Chen, T. Wang, J. Jie, H. Kang, Y. Zhang, S. Guo, H. Ruan, Y. Zhao, Z. Cao, T. Li, et al., Directly cast bulk eutectic and near-eutectic high entropy alloys with balanced strength and ductility in a wide temperature range, Acta Materialia 124 (2017) 143–150, doi:10.1016/j.actamat.2016.11.016.
[10] Y. Zhang, J. Li, X. Wang, Y. Lu, Y. Zhou, X. Sun, et al., The interaction and migration of deformation twin in an eutectic high-entropy alloy $AlCoCrFeNi_{2.1}$, Journal of Materials Science and Technology 35 (5) (2019) 902–906, doi:10.1016/j.jmst.2018.09.067.
[11] S. Muskeri, V. Hasannaeimi, R. Salloom, M. Sadeghilaridjani, S. Mukherjee, et al., Small-scale mechanical behavior of a eutectic high entropy alloy, Scientific Reports 10 (1) (2020) 2669, doi:10.1038/s41598-020-59513-2.
[12] X. Gao, Y. Lu, B. Zhang, N. Liang, G. Wu, G. Sha, J. Liu, Y. Zhao, Microstructural origins of high strength and high ductility in an $AlCoCrFeNi_{2.1}$ eutectic high-entropy alloy, Acta Materialia 141 (2017) 59–66.
[13] N.R. Jaladurgam, A. Lozinko, S. Guo, T.-L. Lee, M.H. Colliander, et al., Temperature dependent load partitioning and slip mode transition in a eutectic $AlCoCrFeNi_{2.1}$ high entropy alloy, Materialia 17 (2021) 101118, doi:10.1016/j.mtla.2021.101118.
[14] L. Wang, C. Yao, J. Shen, Y. Zhang, T. Wang, Y. Ge, L. Gao, G. Zhang, Microstructures and room temperature tensile properties of as-cast and directionally solidified $AlCoCrFeNi_{2.1}$ eutectic high-entropy alloy, Intermetallics 118 (2020) 106681.
[15] S. Harjo, T. Ito, K. Aizawa, H. Arima, J. Abe, A. Moriai, T. Iwahashi, T. Kamiyama, et al., Current Status of Engineering Materials Diffractometer at J-PARC, Materials Science Forum 681 (September 2008) (2011) 443–448. https://www.scientific.net/MSF.681.443
[16] B.H. Toby, R.B. Von Dreele, IUCr, GSAS-II : the genesis of a modern open-source all purpose crystallography software package, Journal of Applied Crystallography 46 (2) (2013) 544–549, doi:10.1107/S0021889813003531.
[17] M.R. Daymond, The determination of a continuum mechanics equivalent elastic strain from the analysis of multiple diffraction peaks, Journal of applied physics 96 (8) (2004) 4263–4272.
[18] M.Z. Ahmed, K. Chadha, S.R. Reddy, D. Shahriari, P.P. Bhattacharjee, M. Jahazi, Influence of Process Parameters on Microstructure Evolution During Hot Deformation of a Eutectic High-Entropy Alloy (EHEA), Metallurgical and Materials Transactions A: Physical Metallurgy and Materials Science 51 (12) (2020) 6406–6420, doi:10.1007/s11661-020-05991-y.
[19] B.E. Warren, X-Ray Diffraction, Dover Publications (New York), 1990, pp. 254–314.
[20] Y. Wang, B. Liu, K. Yan, M. Wang, S. Kabra, Y.L. Chiu, D. Dye, P.D. Lee, Y. Liu, B. Cai, Probing deformation mechanisms of a FeCoCrNi high-entropy alloy at 293 and 77 K using in situ neutron diffraction, Acta Materialia 154 (2018) 79–89, doi:10.1016/j.actamat.2018.05.013.